Nanoscale

PAPER

View Article Online
View Journal | View Issue

Cite this: *Nanoscale*, 2016, **8**, 11698

Long-chain amine-templated synthesis of gallium sulfide and gallium selenide nanotubes†

A. Seral-Ascaso,[a,b] S. Metel,[a,c] A. Pokle,[a,b] C. Backes,[a,b] C. J. Zhang,[a,c] H. C. Nerl,[a,b] K. Rode,[a,b] N. C. Berner,[a,c] C. Downing,[a] N. McEvoy,[a,c] E. Muñoz,[d] A. Harvey,[a,b] Z. Gholamvand,[a,b] G. S. Duesberg,[a,c] J. N. Coleman[a,b] and V. Nicolosi*[a,b,c]

Received 27th February 2016,
Accepted 16th May 2016

DOI: 10.1039/c6nr01663d

www.rsc.org/nanoscale

We describe the soft chemistry synthesis of amine-templated gallium chalcogenide nanotubes through the reaction of gallium(III) acetylacetonate and the chalcogen (sulfur, selenium) using a mixture of long-chain amines (hexadecylamine and dodecylamine) as a solvent. Beyond their role as solvent, the amines also act as a template, directing the growth of discrete units with a one-dimensional multilayer tubular nanostructure. These new materials, which broaden the family of amine-stabilized gallium chalcogenides, can be tentatively classified as direct large band gap semiconductors. Their preliminary performance as active material for electrodes in lithium ion batteries has also been tested, demonstrating great potential in energy storage field even without optimization.

Introduction

During the past decades, one-dimensional (1D) nanostructures have greatly attracted the attention of the research community due to their exclusive properties arising from their small size and tubular shape, allowing promising applications from nanoelectronics to biomedicine.[1–4]

Following the interest generated by the first reports on carbon nanotubes,[5] the field of 1D materials quickly expanded to the synthesis of the inorganic counterparts, including transition metal chalcogenides, oxides and halides, among others.[5–12] Interesting enough, nanotubes of gallium oxide and gallium nitride exhibiting semiconducting properties were also reported.[13,14]

Different synthesis methods of inorganic nanotubes include high-temperature routes, such as chemical vapour deposition, laser ablation and atomic layer deposition,[14–20] as well as low-temperature processes, *i.e.* hydrothermal and sol–gel methods (so-called soft-chemistry).[21–25] The latter have also been extended to the synthesis of 1D nanostructures composed by organic and inorganic moieties, including long-chain amine-templated vanadium oxide,[9] vanadium sulfide[26] and copper sulfide nanotubes.[27]

Usually, long-chain amines are utilized as a template for the growth of hybrid nanotubes due to their ability for self-assembly, arising from the combination of a strongly-polar amino group and a non-polar long hydrocarbon chain.[28] Aromatic and short-chain amines have been successfully utilized for the soft-chemistry preparation of different gallium chalcogenide superstructures, usually forming crystalline frameworks composed of layers, chains or even helical tubes with interesting properties such as high surface area, or ion exchange capability.[29–33] However, to the best of our knowledge, the ability of long-chain amines to direct the growth of 1D nanostructures in the gallium/chalcogens system has never been studied and still remains an important challenge in the field.

Herein, we report the soft-chemistry synthesis of long-chain amine-templated gallium chalcogenide (sulfur, selenium) nanotubes, using a mixture of dodecylamine and hexadecylamine as a solvent and growth template (Scheme 1). The synthesis conditions were studied and optimized to produce high

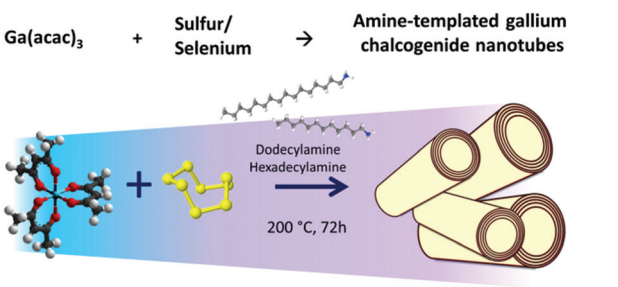

Scheme 1 Illustration of the synthesis reaction of amine-templated gallium chalcogenide nanotubes.

[a]*CRANN & AMBER, Trinity College Dublin, Pearse Street, Dublin 2, Ireland. E-mail: Nicolov@tcd.ie*
[b]*School of Physics, Trinity College Dublin, College Green, Dublin 2, Ireland*
[c]*School of Chemistry, Trinity College Dublin, College Green, Dublin 2, Ireland*
[d]*Instituto de Carboquímica ICB-CSIC, Miguel Luesma Castán 4, 50018 Zaragoza, Spain*

†Electronic supplementary information (ESI) available. See DOI: 10.1039/c6nr01663d

purity materials with a maximum yield of nanotubes up to 70%. Moreover, preliminary studies showed a promising performance of these materials when used as active constituents in electrodes for lithium ion batteries.

Results and discussion

Scanning electron microscopy (SEM) of the synthesized materials (Fig. 1a and b) shows the presence of hollow, tubular structures with lengths between 100 and 500 nm in the case of the amine-templated gallium sulfide nanotubes (A_tGaS_x-NTs) and in the range of 100 nm to 2 μm for the amine-templated gallium selenide nanotubes (A_tGaSe_y-NTs). Low-magnification transmission electron microscopy (TEM) shows single nanotubes and bundled nanotubes in both cases, with a multi-walled structure, usually with open caps and terminating in a circular shape (Fig. 1c–f). However, at this stage, it is unclear whether they consist of concentric tubes or scrolled sheets.

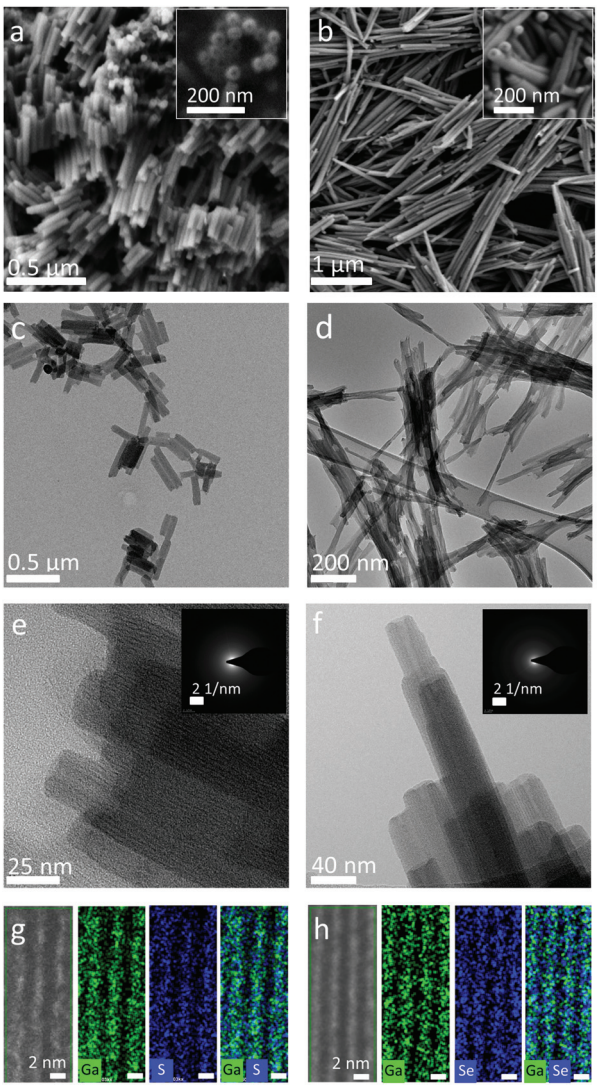

Fig. 1 SEM micrographs of A_tGaS_x-NTs (a) and A_tGaSe_y-NTs (b). A detail of the hollow cores of the nanotubes is shown in the insets. TEM micrographs of A_tGaS_x-NTs (c) and A_tGaSe_y-NTs (d) as seen at low magnification. Details of open edges, parallel walls and empty inner part of the A_tGaS_x-NTs (e) and A_tGaSe_y-NTs (f). Selected area electron diffraction patterns of the corresponding tubes are presented as inset in (e) and (f). High resolution EDX mapping of the A_tGaS_x-NTs (g) and A_tGaSe_y-NTs (h). From left to right (in both images): HAADF-STEM image of the nanotubes, EDX mapping of gallium, EDX mapping of the chalcogen and EDX mapping of the gallium and the chalcogen together.

The observed interlayer distances between the parallel stacked walls of the nanotubes are 29.1 Å and 25.0 Å on average in the case of the sulfur- and selenium-based nanotubes, respectively (Fig. S1 in ESI†), significantly greater than the interlayer distances commonly found in inorganic nanotubes[34,35] but similar to those observed in nanotubes with intercalated long-chain amines.[28] This finding indicates that the amines used as solvent (hexadecylamine and dodecylamine) are effectively incorporated into the tube structure and most likely act as a template for structure growth, as previously reported for nanotubes of vanadium oxide, vanadium sulfide and metallophosphates.[9,28,36] The tubes exhibit very poor crystallinity under high-resolution TEM (see selected area electron diffraction patterns in the insets in Fig. 1e and f). Their structure is damaged within seconds upon exposure to the electron beam and the nanotubes noticeably shrink.

The TEM energy dispersive X-ray spectroscopy (EDX) analysis of the nanotubes shows peaks at the characteristic energies of carbon, gallium and sulfur/selenium (Fig. S2 in ESI†). Oxygen is also detected in both samples; it constituted a small shoulder in the case of A_tGaS_x-NTs and a more prominent peak in the A_tGaSe_y-NTs. The presence of oxygen is likely due to the incorporation of this element during synthesis or a partial oxidation of the tubes when exposed to air during post-synthesis processing. Although nitrogen would be expected from the potentially incorporated amine solvent, EDX cannot unambiguously prove the presence of this element due to its intrinsic detection limits and mostly to the fact that the involved signals would overlap with the carbon and oxygen peaks. High resolution EDX mapping, performed in an aberration-corrected Nion UltraSTEM200 microscope, confirms that the parallel layers observed in the TEM are composed of gallium chalcogenides (Fig. 1g and h). The distribution of gallium (green) and sulfur/selenium (blue) clearly overlaps the region where the layers are observed in the high-angle annular dark-field (HAADF) images (black & white), acquired by scanning transmission electron microscopy (STEM) mode. The homogeneous distribution of the elements in the nanotubes and the uniform composition of the samples are confirmed by EDX mapping performed in SEM (Fig. 2a for the A_tGaSe_y-NTs and S3 in ESI† for the A_tGaS_x-NTs).

The powder-X-ray diffraction (XRD) patterns of the nanotubes resemble those of long-chain amine-intercalated layered structures,[37–39] showing multiple peaks due to the 00*l* reflections (Fig. 2b). The basis distance responsible for these harmonics is determined by plotting the inverse of the measured *d*-spacing for these peaks against the order of the harmonic,

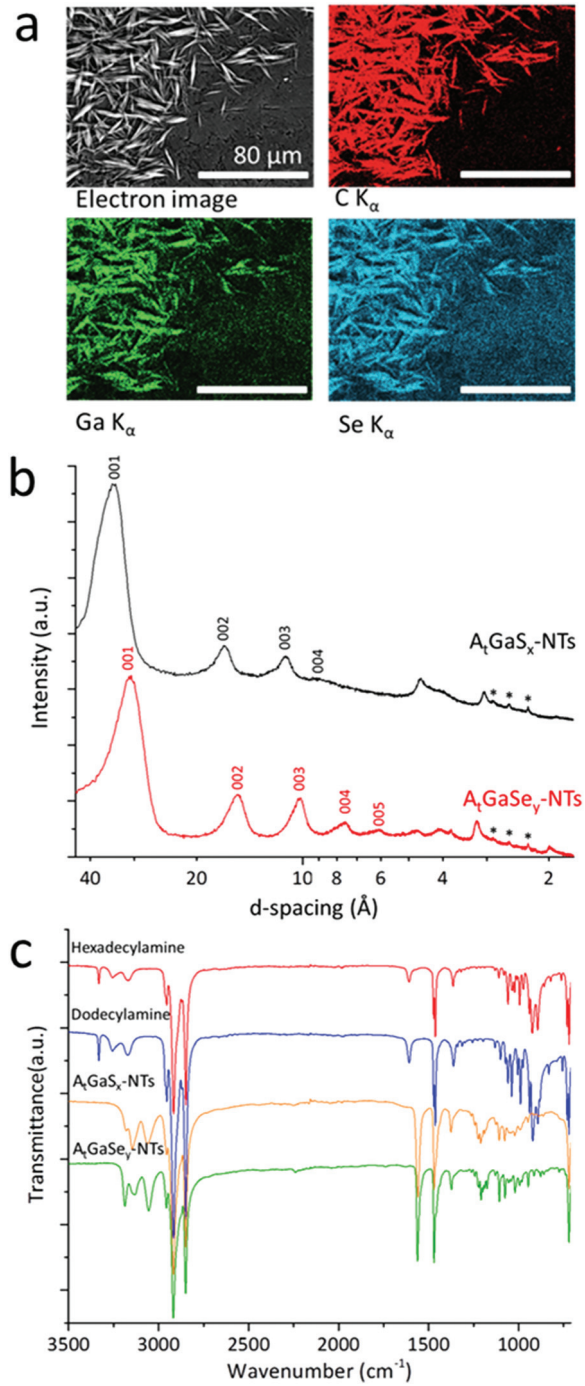

Fig. 2 EDX mapping of A_tGaSe_y-NTs, showing the homogeneous distribution of gallium, selenium and carbon thought the sample (a). XRD patterns of the nanotubes (b); A_tGaS_x-NTs (black line) and A_tGaSe_y-NTs (red line). Peaks marked with * are instrumental artefacts. Comparison of the FT-IR spectra of neat amines and nanotubes (c). The spectra are offset for clarity.

n, which leads to the calculation of the interlayer distance as the reciprocal of the slope of this plot.

The interlayer distances thus calculated are 34.1 Å for the A_tGaS_x-NTs and 30.3 Å for the selenium-based counterparts, similar to that observed in materials containing interlayer hexadecylamine[26,37] and slightly higher than that observed by the TEM (29.1 and 25.0 Å, respectively). The shrinkage observed when the tubes are exposed to the electron beam likely explains the difference in the interlayer distance measured by XRD and TEM.

Some broad peaks and shoulders are observed in the region of *d*-spacing of 3.7 to 4.6 Å in both samples, which can be ascribed to liquid crystal arrangement of the long-chain amines.[37,38] In the sulfur-based sample, a small, broad peak consistent with the poor crystalline quality suggested by TEM, is observed at a *d*-spacing of 3.05 Å, which is similar to the gallium–gallium distance found in other gallium sulfide structures[40] and may correspond to the intralayer distance of the gallium–gallium atoms in the nanotubes. In the A_tGaSe_y-NTs sample, a similar peak is observed at a *d*-spacing of 3.20 Å. Moreover, a broad peak corresponding to a *d*-spacing of 2.00 Å is observed in the A_tGaSe_y-NTs sample, which is similar to interatomic distances commonly reported for gallium–nitrogen bonding in amine-stabilized gallium chalcogenides.[41,42]

Fig. 2c shows a comparison of the Fourier transform infrared (FT-IR) spectra of the nanotubes and the neat amines, clearly indicating the presence of the latter in the tubes and providing interesting structural information. To simplify the data analysis, the bands are analyzed in two groups: vibrational modes involving the nitrogen atom of the amines and vibrational modes involving only the hydrocarbon backbone.

The spectra of both dodecylamine and hexadecylamine present three bands at 3333, 3258 and 3172 cm^{-1}, attributed to the asymmetric and symmetric nitrogen–hydrogen stretching modes and to the symmetric stretching mode interacting with the amine group bending mode, respectively. A scissoring bending mode is observed at 1609 cm^{-1} and a nitrogen–hydrogen wagging band is observed in the region around 925 cm^{-1}.[43,44]

In the FT-IR spectrum of the nanotubes, these vibrational modes are shifted to a lower wavenumber and broadened (both for stretching and scissoring vibrations) or are not observed (wagging), which points to a strong interaction between the amines and gallium chalcogenide structure through the amino group.[43–45]

Moreover, all the bands ascribed to vibrations of the hydrocarbon backbone, including methylene and methyl stretching in the region of 3954–3848 cm^{-1}, the bending modes at 1467, 1386 and 1362 cm^{-1} and the methylene rocking vibration at 718 cm^{-1} (ref. 45) are at the same position in both the amines and nanotubes spectra (Fig. 2c).

Thermogravimetric analysis (TGA) reveals a weight loss of 70.8% and 78.1% for the A_tGaS_x-NTs and A_tGaSe_y-NTs, respectively, when the sample was heated up to 850 °C under air atmosphere (Fig. S4 in ESI†). The analysis of the TGA residues by EDX (SEM) and XRD (Fig. S5 in ESI†) proves that the amines and the sulfur/selenium were removed and only gallium remains as gallium(III) oxide, which allows the estimation of the gallium content in the nanotubes as 21.7% and 16.3% in weight, respectively. Furthermore, the gallium to

chalcogen ratios are calculated using the proportion between the concentrations of the elements obtained by total-reflection X-ray fluorescence (TXRF), based on the signal relative to cobalt, used as an internal standard (Fig. S6 in ESI†), which yields an approximate weight content of the chalcogens in the nanotubes of 12.7% sulfur and 27.6% selenium.

X-ray photoelectron spectroscopy (XPS) survey spectra of the nanotubes are shown in Fig. S7 (ESI†). In both cases, the nitrogen peak is observed at binding energies typical of amines (399.9 eV), and a small contribution from protonated amines is also detected in the A_tGaSe_y-NTs, at binding energies of 401.1 eV (ref. 46) (Fig. S8a in ESI†). In order to study the chemical-bonding environment of gallium and chalcogens, the Ga 3d, S 2p and Se 3d core-level regions were acquired at high resolution. The Ga 3d peak was fitted with two doublets in both samples (Fig. S8b in ESI†), whose binding energies are 18.8 eV and 20.6 eV in the sulfur-based sample and 19.9 eV and 20.4 eV in the selenium-based sample. All these components have a full width at half maximum (FWHM) significantly higher than the resolution of the XPS system, which suggests that each of them comprises a variety of slightly different chemical species. The main components at lower binding energies are most likely associated with gallium bonding to the respective chalcogen,[47] whereas the smaller component lies in the binding energy region which is typical for gallium oxide species.[48] Due to the surface sensitivity of XPS, it is not unlikely that the surface of the A_tGaSe_y-NTs oxidizes during the processing or sample preparation, thus also indicates that the A_tGaSe_y-NTs sample is more sensitive to ambient factors than the sulfur-based counterpart.

In the A_tGaS_x-NTs, the S 2p core-level line shows a significant overlap with the Ga 3s peak, which made the fitting process more challenging. The S 2p and Ga 3s region yield a good fit for only one discernible sulfur component associated with Ga_xS_y species, although with a high FWHM similar to the corresponding Ga 3d component (Fig. S8c in ESI†). Furthermore, the Se 3d region in the A_tGaSe_y-NTs shows interesting features, such as a broad peak which was fitted to two doublets with binding energies of 53.9 eV and 54.4 eV. The first doublet is most probably related to Ga_xSe_y species, while the second one is associated with edge effects or the presence of selenium-enriched regions in sample surface (Fig. S8d in ESI†).

The chemistry of amine-stabilized gallium chalcogenides has been extensively studied during the last decades. These compounds usually present an open-framework structure consisting of the assembly of building blocks composed of corner-linked chains or clusters of the type $[Ga_{10}S_{18}]^{6-}$, $[Ga_{20}S_{35.5}(S_3)_{0.5}O]^{12-}$ or $[GaSe_2]^-_n$, among others.[30,49,50]

Furthermore, direct bonding was reported between gallium and nitrogen atoms in some of these clusters, where sulfur in tetrahedral "GaS_4" units has been partially substituted by a nitrogen from amine ligands to form "GaS_3N" or "GaS_2N_2" units.[31] Moreover, some of these compounds are stabilized by the presence of sulfur–sulfur or selenium–selenium bridging units,[30,50,51] and the negative charge in the clusters or chains is usually compensated with divalent metals or protonated amines.[31,52] In our case, a certain degree of amine protonation is only detected in the A_tGaSe_y-NTs.

In the present study, we propose a structure of layers of polymeric gallium sulfide/selenide alternating with long-chain amines layers. The amines act as the template and scaffold for the nanotube formation and interact with the gallium chalcogenide through the amino group, stabilizing the whole structure in a tubular-like shape resulting in the observed discrete units of multi-walled nanotubes. The gallium chalcogenide layers present a complex structure with a resulting low crystallinity, which incorporates some oxygen, at least in the sample surface.

We must point here that, as suggested by XPS, the A_tGaSe_y-NTs are sensitive to air and moisture and samples of this material are observed to turn reddish when exposed to air. A detailed analysis of an aged sample by SEM (Fig. S9 in ESI†) shows that the nanotubes produce spherical particles composed of selenium, apparently segregated from the nanotubes edges. Further studies to fully characterize the ageing of both materials are currently ongoing.

Optical properties of the nanotubes

To gain insights in the optical properties of the inorganic nanotubes, the dispersions were subjected to absorbance and photoluminescence (PL) spectroscopy. The absorption spectra were measured using an integrating sphere and are presented on the energy scale in Fig. 3a and b. Typically, UV-vis extinction spectra are recorded in transmission mode. However, due to the scattering of nanomaterial dispersions,[53–55] these can mask faint features, as illustrated in Fig. 3a and b, which show absorbance, extinction and scattering spectra of the samples

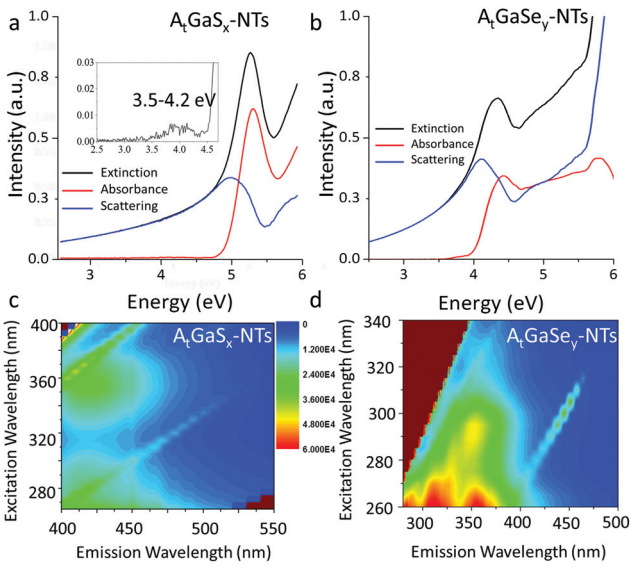

Fig. 3 Optical properties of the nanotubes dispersed in isopropyl alcohol: absorbance (blue line), extinction (black line) and scattering spectra (red line) of the A_tGaS_x-NTs (a) and A_tGaSe_y-NTs (b). The scattering spectrum was calculated as extinction-absorbance. Photoluminescence (PL) excitation-emission contour plot of the dispersions are shown in graphs (c) and (d), respectively.

(N.B. The scattering spectra were obtained by subtracting the absorbance spectrum from the extinction spectrum).

In the A_tGaS_x-NTs, two bands are observed in the UV region: a first high-intensity band, with maximum absorption at 5.2 eV (245 nm), and a second low-intensity transition centred at 3.8 eV (320 nm), while the A_tGaSe_y-NTs show a number of peaks in the UV region at energies >4 eV (310 nm), with the lowest energy absorbance feature centred at 4.4 eV (282 nm) (Fig. 3b). No residual absorbance or transitions are observed in the visible region (lower band gaps) in both samples, since all the signals in the extinction spectra in this spectral region are due to scattering rather than absorbance.

The spectral profile of the nanotubes resembles that of exfoliated gallium(II) chalcogenides nanosheets,[55,56] albeit with the transitions shifted to higher energies, which strongly suggests that, similar to the two-dimensional analogues, the optical absorbance spectra are likely related to excitonic transitions. Since we cannot estimate typical binding energies of the excitons, it was not possible to extract the real band gap from the optical spectra, although it must be larger than the energy of the highest energy transition observed, *e.g.* >5.2 eV for the A_tGaS_x-NTs and >4.4 eV for the A_tGaSe_y-NTs. These values are significantly larger than the band gap of bulk gallium chalcogenides, with values in the range of 2.1–3.3 eV (ref. 56–58) and also larger than the values reported for amine-stabilized gallium chalcogenides, with band gaps in the range of 2.6–4.2 eV and 1.4–2.4 eV for the amine-stabilized gallium sulfides[50,52,59,60] and selenides,[41,42,61] respectively. The increase in the band gap of the nanotubes in comparison to their gallium chalcogenide counterparts, such as GaS or Ga_2Se_3, is coherent with similar results described for amine-intercalated II–VI semiconductor nanostructures and MO_3 (M = Mo, W). These materials in fact present a strong structure-induced quantum effect confinement, which leads to a blue-shift in the absorption edges and a corresponding bandgap increase in the range of 1.0–2.2 eV in respect to the corresponding 3D phases.[62,63] In addition, our nanotubes are expected to have a further quantum confinement contribution due to their curved morphology.

To test whether the materials are a direct band gap semiconductor, the dispersions were subjected to PL spectroscopy, yielding a strong luminescence in both samples (Fig. 3c and d). A_tGaS_x-NTs show an emission centred at 425 nm (2.92 eV). The excitation profile follows the absorbance spectrum, with a red shift of ~0.2 eV, so that a significantly greater luminescence would be expected when exciting further in the UV region where the main absorbance band is centred. However, due to the restrictions of the excitation source (450 W Xenon arc lamp covering a range of 250–1000 nm), this could not be experimentally confirmed. The A_tGaSe_y-NTs display multiple emission features at excitations <300 nm (4 eV) consistent with excitation into the lowest energy absorbance feature. The main emissions are detected at ~290, 315 and 350 nm (4.3, 3.9 and 3.5 eV) which are red-shifted compared to the absorbance. Hence, the emission wavelengths of the tested materials are similar to that of open-framework gallium chalcogenides, which are typically luminescent in the range of 440–500 nm.[30]

In summary, the optical characterization shows that the amine-stabilized gallium chalcogenide nanotubes are distinct from both bulk gallium chalcogenides and other amine-stabilized gallium chalcogenides structures. The materials exhibit excitonic transitions in the UV range and intense PL, which strongly suggests that can be tentatively classified as direct large band gap semiconductors.

Application of the nanotubes in energy storage

To test the future application of the as-synthesized nanotubes in energy storage devices, the nanotubes were processed into composite electrodes and used for lithium ion batteries anodes. Due to the semiconducting nature of the synthesized nanotubes, single-walled carbon nanotubes (SWCNT) were added to improve the conductivity of the electrodes. The composites prepared are denoted as A_tGaS_x-NTs/SWCNT and A_tGaSe_y-NTs/SWCNT, respectively.

The electrochemical performances were evaluated through galvanostatic charge/discharge tests (the curves obtained at 10 mA g^{-1} for both composites are shown in Fig. 4a and b). The initial discharge capacities of A_tGaS_x-NTs/SWCNT and A_tGaSe_y-NTs/SWCNT composites are 190 and 164 mA h g^{-1}, respectively. However, in the A_tGaS_x-NTs/SWCNT, the capacities substantially decrease to 113 mA h g^{-1} at the fifth cycle (Fig. 4a). The apparent capacity loss after the initial several cycles could be attributed to the irreversible formation of solid-electrolyte interphase layer, which caused the consumption of electrolyte, forming a passive layer and lowering down the coulombic efficiency.[64] Similar results were found in the A_tGaSe_y-NTs/SWCNT (Fig. 4b). Since the amine-templated

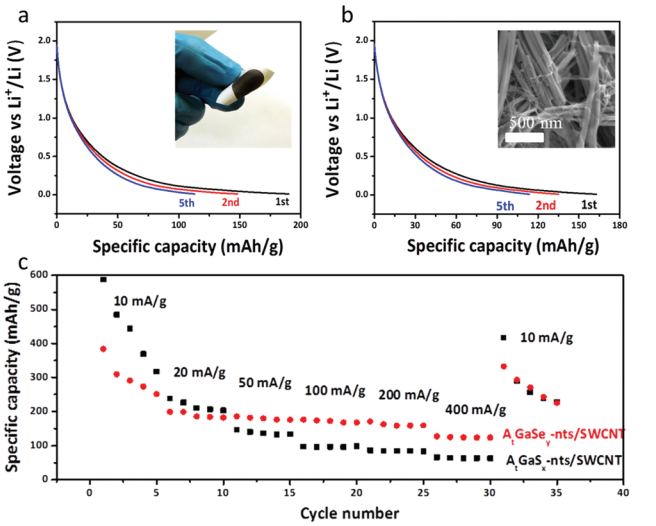

Fig. 4 Discharge curve of A_tGaS_x-NTs/SWCNT (a) and A_tGaSe_y-NTs/SWCNT (b) and rate performances of the electrodes (c). Inset in (a) shows a picture of the flexible A_tGaS_x-NTs/SWCNT electrodes while inset in (b) is a SEM image showing the homogeneous mixing between A_tGaSe_y-NTs and SWCNT in the electrode.

gallium chalcogenide nanotubes were homogeneously distributed onto the conductive SWCNT scaffold, as shown in Fig. 4b (inset), the as-formed void space as well as the open channels in the tubes greatly shortened the Li^+ diffusion into the active sites.

Fig. 4c shows the rate performances of the A_tGaS_x-NTs/SWCNT and A_tGaSe_y-NTs/SWCNT at various current densities. Generally, the capacities of composite films were much higher than SWCNT and amine electrodes at all current densities.

In order to quantitatively determine the specific capacities of the gallium chalcogenide species in the composite electrodes, we subtracted the contribution of SWCNT and amine from the composite, obtaining 317 mA h g^{-1} and 251 mA h g^{-1} at 10 mA g^{-1} for the A_tGaS_x-NTs/SWCNT and A_tGaSe_y-NTs/SWCNT, respectively. Even at 400 mA g^{-1}, the A_tGaSe_y-NTs/SWCNT reached 124 mA h g^{-1}, higher than A_tGaS_x-NTs/SWCNT (63 mA h g^{-1}). The authors are aware that these results are below the performance reported for gallium sulfide deposited on carbon nanotubes (which reached up to 575 mA h g^{-1} at a current density of 120 mA g^{-1} in a voltage window of 0.01–2 V).[65] This is probably due to the presence of encapsulated amines, which effectively might hinder the charge and ion exchange in between the gallium chalcogenide layers. However, it's worth noting that this is an early stage report focused on the synthesis of the amine-templated gallium chalcogenide nanotubes. It is nevertheless interesting to see the described electrochemical behaviour; we believe there is much scope to further enhance the hereby reported electrochemical performance by gaining deep understanding on the multiple redox reactions involved to reach higher capacity (*i.e.* various valence states exist in gallium and chalcogens). Although the optimization of the performance of these materials is out of the scope of this work, these promising results encourage the study of other amine-templated gallium chalcogenide nanostructures with lower amine weight content.

Conclusion

The synthesis of long-chain amine-templated gallium chalcogenide (sulfur, selenium) nanotubes was demonstrated and optimized. The nanotubes were prepared by a soft-chemical route, producing high purity nanotubes with yields as high as 70%.

These new materials belong to the family of amine-stabilized gallium chalcogenides and have a proposed structure composed of alternating layers of long-chain amines and polymeric gallium sulfide/selenide, conforming to a multi-walled tubular structure.

The aspect ratio of the nanotubes is high, with maximum lengths of up to 500 nm for A_tGaS_x-NTs and 2 μm for the A_tGaSe_y-NTs counterparts. Optical characterization indicates that the materials can be tentatively classified as direct large band gap semiconductors, with excitonic transitions in the UV region, which makes them promising for electro-optical applications and studies of quantum effects in semiconducting materials.

The performance of the nanotubes as active material for lithium ion batteries anodes was tested. Results showed values in the range of 251–317 mA h g^{-1} at 10 mA g^{-1} based on the gallium chalcogenide content.

It is envisaged that the versatile soft-chemistry route described here may enable the synthesis of hybrid metal(II)-doped long-chain amine-stabilized gallium chalcogenide frameworks with 1D structure and outstanding functionalities.

Methods

Materials

Gallium(III) acetylacetonate ($Ga(acac)_3$) (99.999%), sulfur (99.99%), selenium (99.5%), hexadecylamine (90%, technical grade), dodecylamine (98%), toluene (99.8%, anhydrous) and isopropyl alcohol (99.5%, anhydrous) were purchased from Sigma Aldrich and stored in a moisture-free atmosphere until use. Single-walled carbon nanotubes were purchased from Carbon Solutions Inc. and used as received.

Synthesis of the nanotubes

The synthesis conditions of the amine-templated gallium chalcogenide nanotubes, such as temperature, chalcogenide to gallium starting molar ratio, reaction time and type of chalcogenide precursor, were optimized (see section 1 in ESI†) and are described below: 1 mmol of $Ga(acac)_3$ and 2 mmol of sulfur (or 1.5 mmol of selenium) were added to a two-neck 100 cm^3 flask containing a degassed mixture of 100 mmol of hexadecylamine and 20 mmol of dodecylamine. The mixture was heated to 150 °C under nitrogen atmosphere for 1 h. The temperature was then increased to 200 °C and the reaction was carried out for 72 h.

After the reaction, the system was naturally cooled down and 10 cm^3 of toluene were added into the reaction flask to facilitate the washing of the obtained precipitate, which was performed by using 80 cm^3 of anhydrous isopropyl alcohol previously heated to 70 °C, followed by centrifugation (425*g*, 5 min), repeated three times. The solid was re-dispersed in 100 cm^3 of isopropyl alcohol by mild sonication and filtered to remove impurities, and then centrifuged (1700*g*, 5 min) to precipitate the white solid.

Characterization techniques

SEM images were acquired using a Zeiss Ultra Plus field-emission microscope equipped with a Gemini® column and a secondary electron detector, working at acceleration voltages in the range of 2–5 kV. TEM images were taken using a FEI Titan microscope operated at accelerating voltages of 80 kV. STEM analysis was performed using a NION Ultra STEM 200 operating at 200 kV with a Bruker windowless EDX detector. EDX analyses were performed with the microscopes operating at 15 kV (SEM), 80 kV (TEM) and 200 kV (Nion) and analyzed with INCA and TIA softwares, respectively.

XRD was performed in a Siemens D500 X-ray diffractometer equipped with a Cu K_α emission source (λ = 1.5418 Å) in the

Bragg–Brentano configuration (2θ angle from 2–60 degrees, step 0.02 degrees). To avoid sample decomposition, the A_tGaSe_y-NTs were coated with a very thin film of parafilm to protect them from oxygen and moisture. TXRF analysis[66,67] was performed with a S2 PicoFox TXRF spectrometer from Bruker Nano GmbH, equipped with a molybdenum X-ray source working at 50 kV and 600 μA, a multilayer monochromator with 80% of reflectivity at 17.5 keV (Mo Kα), a XFlash SDD detector with an effective area of 30 mm^2 and an energy resolution better than 150 eV for Mn Kα. Cobalt was used as an internal standard. XPS spectra were taken using monochromated Al Kα X-rays from an Omicron XM1000 MkII X-ray source and an Omicron EA125 energy analyzer. The analyzer pass energies were 15 eV for the core-level spectra and 100 eV for the survey spectra. An Omicron CN10 electron flood gun was used for charge compensation. After subtraction of a Shirley background, the core-level spectra were fitted with Gaussian–Lorentzian line shapes using the software CasaXPS.

Optical absorbance was measured from 220 to 800 nm on a Perkin Elmer 650 spectrometer in quartz cuvettes, with a path length of 0.4 cm. Prior to the measurements, the sample was dispersed in isopropyl alcohol by mild sonication. As nanomaterial dispersions typically show scattering, in addition to absorbance,[53,55] the optical absorbance was measured in an integrating sphere. A home-built sample holder was used to place the transparent cuvette in the centre of the sphere. The absorbance spectrum was obtained from measurements inside the sphere, where all the scattered light is collected. This procedure was necessary to reveal subtle and faint features in the spectra that could be masked by the scattering background.[55] A second measurement was conducted in transmission outside the integrating sphere to obtain the extinction spectrum. The scattering spectrum was calculated from both measurements by subtracting the absorbance from the extinction spectrum.

PL of the sample was measured in quartz cuvettes using an Edinburgh Instruments FS920 PL spectrometer equipped with a xenon lamp (450 W) and a S900 photomultiplier tube detector. The contour plot was measured at room temperature using single monochromators to record the excitation and emission. The bandwidth was 5 nm, and the acquisition time was 0.3 s. To avoid dispersion artefacts caused by scattering of the nanomaterial, a 395 nm cut-off filter was placed on the emission side. The excitation was corrected for the light intensity.

FT-IR spectra were recorded in the range of 750–3500 cm^{-1} using a Perkin Elmer Spectrum 100 FT-IR spectrometer. Measurements were carried out by the diffuse reflectance method on the neat samples directly. TGA were carried out using a Perkin Elmer Pyris 1 TGA, which had previously been calibrated with nickel and iron standards, by heating 10 mg of finely ground powder of the sample to 850 °C (rate 10 °C min^{-1}) under air atmosphere.

Electrochemical measurements

Preparation of the electrodes. 12 mg of amine-templated gallium chalcogenide nanotubes were dispersed in anhydrous isopropyl alcohol by sonication in a bath for 30 min, and then mixed with 26 cm^3 of a homogeneous dispersion of 0.1 mg cm^{-3} SWCNT in anhydrous isopropyl alcohol. To allow the complete mixing of the materials, the sample was bath sonicated for an additional 5 min. Following this, the sample was vacuum-filtered through a Celgard K2045 membrane (Coated PP, Celgard LLC, Charlotte, NC) and dried overnight at 100 °C in a vacuum oven, to produce a conductive, free-standing electrode (inset in Fig. 4a).

For the purpose of comparison, a mixture of hexadecylamine and dodecylamine powder (1.0 mmol + 0.2 mmol, respectively) was rolled into film electrode using the traditional method, mixing with conductive agent and polyvinylidene fluoride in *N*-methyl pyrrolidinone. After pestling for 10 min, the homogeneous slurry was gently casted onto the copper foil. The amine film was dried under vacuum and punched into an electrode with a diameter of 12 mm and thickness of 20 μm (excluding the thickness of copper). The electrodes were then transferred to the glove box ready for further use. The SWCNT electrodes were prepared similarly to the composite.

Cell assembly. After an overnight vacuum heating in the oven, the composites were cut into square stripes with a size of 0.7 × 0.7 cm. The thickness and mass of each electrode was 10 μm and 0.6 mg, respectively. CR2032 coin-type cells were assembled using the composite as the working electrode and lithium metal foil as the counter and reference electrode. A porous polypropylene membrane (Celgard K2045) was used as the separator. The electrolyte was 1 M lithium hexafluorophosphate/ethylene carbonate/diethyl carbonate. The cells were assembled in an argon filled glovebox.

Electrochemical characterization. The galvanostatic charge–discharge tests were carried out on an Arbin Potentiostat (BT2145, USA) between 0.01–2 V (*vs.* Li/Li^+) at different current densities, ranging from 10 mA g^{-1} to 500 mA g^{-1}. The cell was cycled 5 times under each current density and the discharge capacity at the fifth cycle was taken as the stable value. Similarly, galvanostatic charge–discharge tests were also conducted on the SWCNT and amine only.

Abbreviations

A_tGaS_x-NTs	Amine-templated gallium sulfide nanotubes
A_tGaSe_y-NTs	Amine-templated gallium selenide nanotubes
SEM	Scanning electron microscopy
TEM	Transmission electron microscopy
EDX	Energy dispersive X-ray spectroscopy
HAADF	High-angle annular dark-field
STEM	Scanning transmission electron microscopy
XRD	X-ray diffraction
TXRF	Total-reflection X-ray fluorescence
XPS	X-ray photoelectron spectroscopy
FWHM	Full width at half maximum
PL	Photoluminescence
FT-IR	Fourier transform infrared

TGA	Thermogravimetric analysis
SWCNT	Single-walled carbon nanotubes

Acknowledgements

This study was been supported by Science Foundation Ireland (SFI) under grant number SFI/12/RC/2278. VN would like to acknowledge the following funding support: SFI AMBER, SFI PIYRA, ERC StG 2DNanoCaps, ERC PoC 2DUSD, ERC PoC 2DInk, EU MC ITN MoWSeS, EU NMP Co-Pilot. NMcE was supported by SFI under 14/TIDA/2329, and NCB and GSD under SFI PI_10/IN.1/I3030. The authors would like to thank Michael Finneran, Trevor Woods and Manuel Ruether from Trinity College Dublin, all the technical staff at the Advanced Microscopy Laboratory in CRANN TCD, and Ramón Fernández-Ruiz and Josué Friedrich from Universidad Autónoma de Madrid, for their support.

References

1 L. Qian, F. Teng, Z. S. Jin, Z. J. Zhang, T. Zhang, Y. B. Hou, S. Y. Yang and X. R. Xu, *J. Phys. Chem. B*, 2004, **108**, 13928–13931.
2 H. Tokudome and M. Miyauchi, *Angew. Chem., Int. Ed.*, 2005, **44**, 1974–1977.
3 G. Lalwani, A. M. Henslee, B. Farshid, P. Parmar, L. J. Lin, Y. X. Qin, F. K. Kasper, A. G. Mikos and B. Sitharaman, *Acta Biomater.*, 2013, **9**, 8365–8373.
4 A. H. Liu, M. D. Wei, I. Honma and H. S. Zhou, *Adv. Funct. Mater.*, 2006, **16**, 371–376.
5 S. Iijima, *Nature*, 1991, **354**, 56–58.
6 R. Tenne, L. Margulis, M. Genut and G. Hodes, *Nature*, 1992, **360**, 444–446.
7 Y. Feldman, E. Wasserman, D. J. Srolovitz and R. Tenne, *Science*, 1995, **267**, 222–225.
8 C. N. R. Rao and M. Nath, *Dalton Trans.*, 2003, 1–24.
9 M. E. Spahr, P. Bitterli, R. Nesper, M. Muller, F. Krumeich and H. U. Nissen, *Angew. Chem., Int. Ed.*, 1998, **37**, 1263–1265.
10 P. Hoyer, *Langmuir*, 1996, **12**, 1411–1413.
11 Y. R. Hacohen, E. Grunbaum, R. Tenne, J. Sloan and J. L. Hutchison, *Nature*, 1998, **395**, 336–337.
12 G. Tourillon, L. Pontonnier, J. P. Levy and V. Langlais, *Electrochem. Solid-State Lett.*, 2000, **3**, 20–23.
13 B. Cheng and E. T. Samulski, *J. Mater. Chem.*, 2001, **11**, 2901–2902.
14 J. Goldberger, R. R. He, Y. F. Zhang, S. W. Lee, H. Q. Yan, H. J. Choi and P. D. Yang, *Nature*, 2003, **422**, 599–602.
15 J. Sha, J. J. Niu, X. Y. Ma, J. Xu, X. B. Zhang, Q. Yang and D. Yang, *Adv. Mater.*, 2002, **14**, 1219–1221.
16 A. Stojanovic, S. Olveira, M. Fischer and S. Seeger, *Chem. Mater.*, 2013, **25**, 2787–2792.
17 D. P. Yu, X. S. Sun, C. S. Lee, I. Bello, S. T. Lee, H. D. Gu, K. M. Leung, G. W. Zhou, Z. F. Dong and Z. Zhang, *Appl. Phys. Lett.*, 1998, **72**, 1966–1968.
18 E. L. Lakomaa, *Appl. Surf. Sci.*, 1994, **75**, 185–196.
19 Y. S. Min, E. J. Bae, K. S. Jeong, Y. J. Cho, J. H. Lee, W. B. Choi and G. S. Park, *Adv. Mater.*, 2003, **15**, 1019–1022.
20 T. Kijima, T. Yoshimura, M. Uota, T. Ikeda, D. Fujikawa, S. Mouri and S. Uoyama, *Angew. Chem., Int. Ed.*, 2004, **43**, 228–232.
21 A. R. Armstrong, J. Canales and P. G. Bruce, *Angew. Chem., Int. Ed.*, 2004, **43**, 4899–4902.
22 S. Mukherjee, V. A. Bartlow and S. Nair, *Chem. Mater.*, 2005, **17**, 4900–4909.
23 X. Y. Liu, J. H. Zeng, S. Y. Zhang, R. B. Zheng, X. M. Liu and Y. T. Qian, *Chem. Phys. Lett.*, 2003, **374**, 348–352.
24 B. Ni, H. Liu, P.-p. Wang, J. He and X. Wang, *Nat. Commun.*, 2015, **6**, 8756.
25 H. Nakamura and Y. Matsui, *J. Am. Chem. Soc.*, 1995, **117**, 2651–2652.
26 F. Krumeich, H.-J. Muhr, M. Niederberger, F. Bieri, B. Schnyder and R. Nesper, *J. Am. Chem. Soc.*, 1999, **121**, 8324–8331.
27 Q. Y. Lu, F. Gao and D. Y. Zhao, *Nano Lett.*, 2002, **2**, 725–728.
28 X. Guo, X. Guo, W. Tao, L. Chen, L. Peng and W. Ding, *Chem. Commun.*, 2011, **47**, 10061–10063.
29 N. F. Zheng, X. G. Bu, B. Wang and P. Y. Feng, *Science*, 2002, **298**, 2366–2369.
30 N. F. Zheng, X. H. Bu and P. Y. Feng, *J. Am. Chem. Soc.*, 2003, **125**, 1138–1139.
31 P. Vaqueiro, *Inorg. Chem.*, 2006, **45**, 4150–4156.
32 S. J. Ewing, M. L. Romero, J. Hutchinson, A. V. Powell and P. Vaqueiro, *Z. Anorg. Allg. Chem.*, 2012, **638**, 2526–2531.
33 P. Vaqueiro, M. L. Romero, B. C. Rowan and B. S. Richards, *Chem. – Eur. J.*, 2010, **16**, 4462–4465.
34 H. A. Therese, J. X. Li, U. Kolb and W. Tremel, *Solid State Sci.*, 2005, **7**, 67–72.
35 J. Cumings and A. Zettl, *Chem. Phys. Lett.*, 2000, **316**, 211–216.
36 H. A. Therese, F. Rocker, A. Reiber, J. X. Li, M. Stepputat, G. Glasser, U. Kolb and W. Tremel, *Angew. Chem., Int. Ed.*, 2005, **44**, 262–265.
37 E. Wortham, B. Bonnet, D. J. Jones, J. Roziere and G. R. Burns, *J. Mater. Chem.*, 2004, **14**, 121–126.
38 T. Jiang and G. A. Ozin, *J. Mater. Chem.*, 1997, **7**, 2213–2222.
39 S. Zhang, Q. F. Liu, H. F. Cheng, X. G. Li, F. G. Zeng and R. L. Frost, *J. Colloid Interface Sci.*, 2014, **430**, 345–350.
40 P. Vaqueiro, *J. Solid State Chem.*, 2006, **179**, 302–307.
41 Y. J. Dong, Q. Peng, R. J. Wang and Y. D. Li, *Inorg. Chem.*, 2003, **42**, 1794–1796.
42 S. J. Ewing and P. Vaqueiro, *Inorg. Chem.*, 2014, **53**, 8845–8847.
43 J. K. Cooper, A. M. Franco, S. Gul, C. Corrado and J. Z. Zhang, *Langmuir*, 2011, **27**, 8486–8493.
44 R. A. Meyers, *Encyclopedia of analytical chemistry: applications, theory, and instrumentation*, Wiley, Chichester; New York, 2000.

45 R. M. Silverstein, F. X. Webster, D. J. Kiemle and D. L. Bryce, *Spectrometric identification of organic compounds*, Wiley, Hoboken, NJ, 2015.
46 N. Graf, E. Yegen, T. Gross, A. Lippitz, W. Weigel, S. Krakert, A. Terfort and W. E. S. Unger, *Surf. Sci.*, 2009, **603**, 2849–2860.
47 F. R. Shepherd and P. M. Williams, *Phys. Rev. B: Condens. Matter*, 1975, **12**, 5705–5713.
48 R. Carli and C. L. Bianchi, *Appl. Surf. Sci.*, 1994, **74**, 99–102.
49 J. Zhou, Y. Zhang, G. Q. Bian, C. Y. Li, X. X. Chen and J. Dai, *Cryst. Growth Des.*, 2008, **8**, 2235–2240.
50 P. Vaqueiro and M. L. Romero, *J. Phys. Chem. Solids*, 2007, **68**, 1239–1243.
51 A. Fehlker, R. Blachnik and H. Reuter, *Z. Anorg. Allg. Chem.*, 1999, **625**, 1225–1228.
52 P. Vaqueiro and M. L. Romero, *J. Am. Chem. Soc.*, 2008, **130**, 9630–9631.
53 C. Backes, R. J. Smith, N. McEvoy, N. C. Berner, D. McCloskey, H. C. Nerl, A. O'Neill, P. J. King, T. Higgins, D. Hanlon, N. Scheuschner, J. Maultzsch, L. Houben, G. S. Duesberg, J. F. Donegan, V. Nicolosi and J. N. Coleman, *Nat. Commun.*, 2014, **5**, 4576.
54 L. Yadgarov, C. L. Choi, A. Sedova, A. Cohen, R. Rosentsveig, O. Bar-Elli, D. Oron, H. J. Dai and R. Tenne, *ACS Nano*, 2014, **8**, 3575–3583.
55 A. Harvey, C. Backes, Z. Gholamvand, D. Hanlon, D. McAteer, H. C. Nerl, E. McGuire, A. Seral-Ascaso, Q. M. Ramasse, N. McEvoy, S. Winters, N. C. Berner, D. McCloskey, J. F. Donegan, G. S. Duesberg, V. Nicolosi and J. N. Coleman, *Chem. Mater.*, 2015, **27**, 3483–3493.
56 K. Allakhverdiev, J. Hagen and Z. Salaeva, *Phys. Status Solidi A*, 1997, **163**, 121–127.
57 M. Springford, *Proc. Phys. Soc., London*, 1963, **82**, 1020–1028.
58 E. Aulich, J. L. Brebner and E. Mooser, *Phys. Status Solidi*, 1969, **31**, 129–131.
59 C. Y. Li, J. Zhou, G. Q. Bian, M. H. Zhang and J. Dai, *Inorg. Chem. Commun.*, 2008, **11**, 1327–1329.
60 P. Vaqueiro and M. L. Romero, *Inorg. Chem.*, 2009, **48**, 810–812.
61 X. H. Bu, N. F. Zheng, X. Q. Wang, B. Wang and P. Y. Feng, *Angew. Chem., Int. Ed.*, 2004, **43**, 1502–1505.
62 X. Y. Huang, J. Li, Y. Zhang and A. Mascarenhas, *J. Am. Chem. Soc.*, 2003, **125**, 7049–7055.
63 X. Zhang, M. Hejazi, S. J. Thiagarajan, W. R. Woerner, D. Banerjee, T. J. Emge, W. Q. Xu, S. J. Teat, Q. H. Gong, A. Safari, R. G. Yang, J. B. Parise and J. Li, *J. Am. Chem. Soc.*, 2013, **135**, 17401–17407.
64 Y. Wei, Y. Tao, C. Zhang, J. Wang, W. Qiao, L. Ling and D. Long, *Electrochim. Acta*, 2016, **188**, 385–392.
65 X. Meng, K. He, D. Su, X. Zhang, C. Sun, Y. Ren, H. H. Wang, W. Weng, L. Trahey and C. P. Canlas, *Adv. Funct. Mater.*, 2014, **24**, 5435–5442.
66 R. Klockenkamper and A. VonBohlen, *Total-Reflection X-Ray Fluorescence Analysis and Related Methods*, 2nd edn, 2015.
67 R. Fernandez-Ruiz, P. Ocon and M. Montiel, *J. Anal. At. Spectrom.*, 2009, **24**, 785–791.